

Numerical Experiments on the Two-step Emergence of Twisted Magnetic Flux Tubes in the Sun

S. Toriumi and T. Yokoyama

Department of Earth and Planetary Science, University of Tokyo, Hongo, Bunkyo-ku,
Tokyo 113-0033, Japan

`toriumi@eps.s.u-tokyo.ac.jp`

Received _____; accepted _____

arXiv:1105.1904v1 [astro-ph.SR] 10 May 2011

ABSTRACT

We present the new results of the two-dimensional numerical experiments on the cross-sectional evolution of a twisted magnetic flux tube rising from the deeper solar convection zone ($-20,000$ km) to the corona through the surface. The initial depth is ten times deeper than most of previous calculations focusing on the flux emergence from the uppermost convection zone. We find that the evolution is illustrated by the two-step process described below: the initial tube rises due to its buoyancy, subject to aerodynamic drag due to the external flow. Because of the azimuthal component of the magnetic field, the tube maintains its coherency and does not deform to become a vortex roll pair. When the flux tube approaches the photosphere and expands sufficiently, the plasma on the rising tube accumulates to suppress the tube's emergence. Therefore, the flux decelerates and extends horizontally beneath the surface. This new finding owes to our large scale simulation calculating simultaneously the dynamics within the interior as well as above the surface. As the magnetic pressure gradient increases around the surface, magnetic buoyancy instability is triggered locally and, as a result, the flux rises further into the solar corona. We also find that the deceleration occurs at a higher altitude than in our previous experiment using magnetic flux sheets (Toriumi and Yokoyama). By conducting parametric studies, we investigate the conditions for the two-step emergence of the rising flux tube: field strength $\gtrsim 1.5 \times 10^4$ G and the twist $\gtrsim 5.0 \times 10^{-4}$ km $^{-1}$ at $-20,000$ km depth.

1. Introduction

Emerging magnetic fluxes are thought to be the source of solar active regions (Parker 1955). It is widely accepted that the emerging flux has a form of an Ω -shaped flux tube. Parker (1975) studied the rise time of a flux tube that emerges due to magnetic buoyancy under the resistance of aerodynamic drag. Schüssler (1979) carried out two-dimensional magnetohydrodynamic (MHD) simulations and found that the cross-section of the emerging flux tube is deformed by the surrounding flows into an “umbrella shape” with a pair of counter-rotating flux rolls, leading to fragmentation of the tube (see also Longcope et al. 1996). After Spruit (1981) introduced the thin-flux-tube (TFT) approximation, the emergence of the flux tube has been studied by using this model without considering the effect of the cross-sectional fragmentation (e.g. D’Silva & Choudhuri 1993; Fan et al. 1993, 1994; Caligari et al. 1995; Moreno-Insertis et al. 1995). Moreno-Insertis & Emonet (1996) and Emonet & Moreno-Insertis (1998) carried out compressible MHD simulations using the twisted flux tube, and found that the azimuthal field can suppress the splitting of the rising tube into two vortex filaments (see also Dorch 2007).

Numerical experiments on the flux emergence above the solar surface have been carried out widely in the last two decades. Shibata et al. (1989) produced a pioneering work on the nonlinear evolution of the undular mode of magnetic buoyancy instability (the Parker instability). The expansion of the magnetic fields into the corona was found to be in a self-similar way. Magara (2001) assumed a twisted magnetic flux tube that rises from the uppermost convection zone to the solar corona. When the apex of his flux tube entered the isothermal (i.e., convectively stable) photosphere, the tube extended horizontally around the surface. The rising tube did not develop a wake with a vortex roll pair, because the initial tube was located just beneath the surface ($z = -1800$ km) and the tube directly entered the photosphere before the wake is formed.

The transition of the rising flux through the solar surface has widely been discussed: the thorough review in this matter is found in Moreno-Insertis (2006). Matsumoto & Shibata (1992) carried out the first three-dimensional study on flux emergence, and, since then, various three-dimensional experiments have been done (e.g. Dorch 1999; Fan 2001; Archontis et al. 2004; Isobe et al. 2005; Murray et al. 2006; Manchester et al. 2004; Galsgaard et al. 2007; Toriumi et al. 2011). Recently, MHD calculations including radiative effect are used to reveal the interaction between flux emergence and the convective motion near the surface (Cheung et al. 2007, 2008; Tortosa-Andreu & Moreno-Insertis 2009). Toroidal flux tubes are also considered as an initial condition to study the dynamics of flux emergence (Hood et al. 2009; MacTaggart & Hood 2009).

The works introduced above can be divided into two groups: one is for the dynamics within the interior from $\sim -200,000$ km to the surface, and the other for the emergence from the uppermost convection zone (a few 1000 km depth) to the corona. An additional experiment is required on the evolution of the emerging flux tube from the deep convection layer to the corona through the surface for the further understanding of the flux emergence in a self-consistent manner (Abbett & Fisher 2003). In this paper, we perform a two-dimensional compressible MHD study on the buoyant twisted magnetic flux tube initially embedded deep in the convection zone ($z = -20,000$ km), of which the depth is the same as our previous study (Toriumi & Yokoyama 2010, hereafter Paper I) and is ten times deeper than most of previous calculations considering the emergence from the uppermost convection zone.

In Paper I, we carried out numerical experiments on the emerging flux sheet, which decelerates in the convection zone and extends horizontally beneath the surface. When the magnetic flux accumulates near the surface due to the successive emergence below, the flux sheet is subject to the Parker instability and thus further evolution to the corona occurs

(the “two-step emergence” model). When the field is too weak, the rising flux cannot evolve further to the corona and remains within the solar interior (“failed emergence”), while, in the case of a strong field, the flux directly emerges to the upper atmosphere without showing a deceleration (“direct emergence”).

The results of the present study are similar to the previous experiments. In the convection zone, the cross-sectional evolution of the flux tube is similar to the papers by Moreno-Insertis & Emonet (1996) and Emonet & Moreno-Insertis (1998). We found that, as the flux tube rises, aerodynamic drag becomes more effective, since the external flow from the apex forms a wake behind the main tube. Also, the emergence above the surface is similar to the calculations by Magara (2001). However, there is an important difference from those papers; the deceleration of the rising tube occurs when the tube is far below the photosphere, and the tube makes a flattened ∇ -shaped structure widely beneath the surface. By conducting an analytic model which includes the effect of the mass pile-up, we confirm that the tube’s deceleration is the consequence of the fluid accumulation between the rising tube and the photosphere. The magnetic flux stretched horizontally beneath the surface becomes magnetic buoyancy-unstable locally so that the second-step emergence to the corona takes place. These features resemble the previous two-step model in Paper I. We also carry out parameter surveys to study the dependence on the initial twist and the field strength.

In the next section (§2), we give a description of the model used in this study, while the results of the numerical experiments are shown in detail in Section 3. In Section 4, we present the results of the parameter study. Finally, in Section 5, we summarize and discuss the results.

2. Numerical Model

2.1. Assumptions and Basic Equations

We consider the buoyant rise of an isolated magnetic flux tube in the stratified ideal gas layers in the (y, z) -plane, where the z -coordinate increases upward. We solve the standard set of ideal MHD equations including constant gravitational acceleration $\mathbf{g} = (0, 0, -g_0)$.

The basic equations are the same as those of Paper I:

$$\frac{\partial \rho}{\partial t} + \nabla \cdot (\rho \mathbf{V}) = 0 , \quad (1)$$

$$\frac{\partial(\rho \mathbf{V})}{\partial t} + \nabla \cdot \left(\rho \mathbf{V} \mathbf{V} + p \mathbf{I} - \frac{\mathbf{B} \mathbf{B}}{4\pi} + \frac{\mathbf{B}^2}{8\pi} \mathbf{I} \right) - \rho \mathbf{g} = 0 , \quad (2)$$

$$\frac{\partial \mathbf{B}}{\partial t} = \nabla \times (\mathbf{V} \times \mathbf{B}) , \quad (3)$$

$$\frac{\partial}{\partial t} \left(\rho U + \frac{1}{2} \rho \mathbf{V}^2 + \frac{\mathbf{B}^2}{8\pi} \right) + \nabla \cdot \left[(\rho U + p + \frac{1}{2} \rho \mathbf{V}^2) \mathbf{V} + \frac{c}{4\pi} \mathbf{E} \times \mathbf{B} \right] - \rho \mathbf{g} \cdot \mathbf{V} = 0 , \quad (4)$$

and

$$U = \frac{1}{\gamma - 1} \frac{p}{\rho} , \quad (5)$$

$$\mathbf{E} = -\frac{1}{c} \mathbf{V} \times \mathbf{B} , \quad (6)$$

$$p = \frac{k_B}{m} \rho T , \quad (7)$$

where U is the internal energy per unit mass, \mathbf{I} is the unit tensor, k_B is the Boltzmann constant, m is the mean molecular mass, and other symbols have their usual meanings. In this study, we carry out so-called 2.5-dimensional numerical simulation, that is, all the physical quantities are independent of x while the x -component of vector quantities (i.e.,

velocity \mathbf{V} and magnetic field \mathbf{B}) is taken into account. We assume a ratio of specific heats, $\gamma = 5/3$.

The normalizing units of length, velocity, time, and density in the simulations are H_0 , C_{s0} , $\tau_0 \equiv H_0/C_{s0}$, and ρ_0 , respectively, where $H_0 = k_B T_0 / (m g_0)$ is the pressure scale height, C_{s0} the sound speed, and ρ_0 the density at the photosphere. The gas pressure, temperature, and magnetic field strength are normalized by the combinations of the units above, i.e., $p_0 = \rho_0 C_{s0}^2$, $T_0 = m C_{s0}^2 / (\gamma k_B)$, and $B_0 = (\rho_0 C_{s0}^2)^{1/2}$, respectively. The gravity is given as $g_0 = C_{s0}^2 / (\gamma H_0)$ by definition. For the comparison of numerical results with observations, we use $H_0 = 200$ km, $C_{s0} = 8$ km s $^{-1}$, $\tau_0 = H_0 / C_{s0} = 25$ s, and $\rho_0 = 1.4 \times 10^{-7}$ g cm $^{-3}$, which are typical values for the solar photosphere and chromosphere. Then, $p_0 = 9.0 \times 10^4$ dyn cm $^{-2}$, $T_0 = 4000$ K, and $B_0 = 300$ G.

2.2. Initial Conditions

The initial background stratification consists of three regions (see e.g. Nozawa et al. 1992): an adiabatically stratified convection zone, a cool isothermal photosphere/chromosphere, and a hot isothermal solar corona. We take $z = 0$ to be the base height of the photosphere, and the initial temperature distribution of the photosphere/chromosphere and the corona ($z \geq 0$) is assumed to be

$$T = T_s(z) \equiv T_{\text{ph}} + (T_{\text{cor}} - T_{\text{ph}}) \{ \tanh [(z - z_{\text{cor}}) / w_{\text{tr}}] + 1 \} / 2, \quad (8)$$

where $T_{\text{ph}} = T_0$ and $T_{\text{cor}} = 100T_0$ are the respective temperatures in the photosphere/chromosphere and the corona, $z_{\text{cor}} = 10H_0$ is the base of the corona, and $w_{\text{tr}} = 0.5H_0$ is the temperature scale height of the transition region. The initial temperature distribution in the convection zone ($z \leq 0$) is described as

$$T = T_s(z) \equiv T_{\text{ph}} - z \left. \frac{dT}{dz} \right|_{\text{ad}}, \quad (9)$$

where

$$\left| \frac{dT}{dz} \right|_{\text{ad}} = \frac{\gamma - 1}{\gamma} \frac{mg_0}{k_B} \quad (10)$$

is the adiabatic temperature gradient, i.e., the initial temperature distribution in the convection zone is adiabatic. On the basis of the temperature distribution above, the initial pressure and density profiles are defined by the equation of static pressure balance:

$$\frac{dp_s(z)}{dz} + \rho_s(z)g_0 = 0. \quad (11)$$

The initial magnetic flux tube is embedded in the solar interior at $z = -100H_0 = -20,000$ km. The longitudinal and azimuthal components of the flux tube are described as follows (see Fan 2001; Archontis et al. 2004; Murray et al. 2006): for $r \equiv [(y - y_{\text{tube}})^2 + (z - z_{\text{tube}})^2]^{1/2}$,

$$B_x(r) = B_{\text{tube}} \exp\left(-\frac{r^2}{R_{\text{tube}}^2}\right), \quad (12)$$

and

$$B_\phi(r) = qrB_x(r), \quad (13)$$

where $(y_{\text{tube}}, z_{\text{tube}}) = (0, -100H_0)$ is the tube center, R_{tube} is the tube radius, q is the twist parameter denoting the angular rate of field lines rotating around the tube's axis per unit length, and B_{tube} is the field strength at the center. The horizontal and vertical components of the azimuthal field are defined as

$$B_y(y, z) = -B_\phi(r) \frac{z - z_{\text{tube}}}{r}, \quad (14)$$

and

$$B_z(y, z) = B_\phi(r) \frac{y - y_{\text{tube}}}{r}, \quad (15)$$

respectively. We use $R_{\text{tube}} = 5H_0 = 1000$ km throughout the paper. For the typical case (case 1), we take $B_{\text{tube}} = 50B_0 = 1.5 \times 10^4$ G, so the total longitudinal magnetic flux is $\Phi_x = 4.7 \times 10^{20}$ Mx. The twist parameter is $q = 0.1/H_0$ for case 1. The pressure inside the tube is defined as

$$p_i(y, z) = p_s(z) + \delta p_{\text{exc}}(r) , \quad (16)$$

where $\delta p_{\text{exc}}(< 0)$ is the pressure excess described as

$$\delta p_{\text{exc}}(r) = \frac{B_x^2(r)}{8\pi} \left[q^2 \left(\frac{R_{\text{tube}}^2}{2} - r^2 \right) - 1 \right] , \quad (17)$$

for the pressure balance. The temperature is kept unchanged, i.e., thermal balance is sustained, $T_i(z) = T_s(z)$. Since the density inside the tube is smaller than that outside, the flux tube will buoyantly rise through the convection zone. The initial temperature, density, and pressure profiles of the background stratification, and the total field strength $B = [B_x^2 + B_\phi^2]^{1/2} = [B_x^2 + B_y^2 + B_z^2]^{1/2}$ of case 1 along $y = 0$ are shown in Figure 1.

2.3. Boundary Conditions and Numerical Procedures

The domain of the simulation box is ($y_{\min} < y < y_{\max}$) and ($z_{\min} < z < z_{\max}$), where $y_{\min} = -400H_0$, $y_{\max} = 400H_0$, $z_{\min} = -150H_0$, and $z_{\max} = 250H_0$. The total size of the simulation box is 160 Mm \times 80 Mm. Periodic boundaries are assumed for $y = y_{\min}$ and $y = y_{\max}$, symmetric boundaries for $z = z_{\min}$ and $z = z_{\max}$. A wave-damping region is attached near the top boundary. The total number of grid points is $(N_y \times N_z) = (1536 \times 1920)$, and the mesh sizes are $\Delta y = 0.52H_0$ and $\Delta z = 0.21H_0$, both of which are uniform. We use the modified Lax-Wendroff scheme version of the CANS (Coordinated Astronomical Numerical Software) code (see Paper I). To study the dependence on the twist and the field strength of the flux tube, we change the values for

the twist parameter q or the axial field strength B_{tube} . The cases we use in this study are summarized in Table 1.

3. Results

Here, we show the results of the typical model (case 1) in which the initial twisted flux tube with $q = 0.1/H_0$ rises through the convection zone to the corona. The evolution within the interior resembles the studies by Moreno-Insertis & Emonet (1996) and Emonet & Moreno-Insertis (1998), and the evolution to the upper atmosphere is similar to Magara (2001). However, the present result is not a simple sum of them; the rising tube decelerates within the interior far below the surface to build a widely flattened magnetic structure.

Figure 2 displays the evolution of the density profile (color contour) in a vertical plane normal to the tube axis, while the solid lines and arrows indicate the magnetic field lines and the velocity vectors, respectively. Figure 2(a) presents the initial state; the flux tube is located at $z/H_0 = -100$ with a circular shape, and begins to emerge because of the buoyancy due to its smaller density relative to the surroundings. Figure 3(a) shows the height-time relations at the top (solid line), the center (dotted line), and the bottom (dashed line) of the emerging tube, while the velocities at these points are presented in Figure 3(b). In the initial phase ($0 < t/\tau_0 < 100$), the flux tube rises due to magnetic buoyancy and the tube’s cross-section almost keeps its original circular shape. Thus, the tube moves up with a constant acceleration rate. In the next phase ($100 < t/\tau_0 < 500$), the aerodynamic drag grows to counteract buoyancy, since the external flow around the tube’s cross-section develops a wake behind the main tube (Figure 2(c)), and the acceleration of the rise velocity is reduced. The azimuthal field of the flux tube resists this deformation and prevents the tube from fragmenting into a counter-rotating vortex pair (the so-called “umbrella shape”

in Schüssler (1979)). During the emergence in the convection zone, the rise velocity of the tube center fluctuates due to the internal torsional oscillation (Figure 3(b); see §3.1). As the flux tube reaches close to the photosphere, it expands horizontally (Figure 2(e)) and its rise speed decreases after $t/\tau_0 = 500$. Eventually, the subsurface flux extends widely in the range of $-100 < y/H_0 < 100$ at $t/\tau_0 = 800$ (Figure 2(f)). When the top of the subphotospheric flux becomes unstable to the magnetic buoyancy instability, further evolution to the corona breaks out (Figures 2(f)-(i); see §3.3). The consequent coronal loop at the time $t/\tau_0 = 980$ has its width $\sim 400H_0 = 80,000$ km and height $\sim 200H_0 = 40,000$ km. The picture of this evolution resembles our previous “two-step emergence” model (Paper I). In the following sections, we will describe some more detailed results, especially on the magnetic and the flow field within the convection zone, the comparison with the analytic model, and the second-step evolution starting at the photosphere.

3.1. Magnetic Fields and Vorticity

To study the flux tube’s emergence in the solar interior, we show the variation of the field configuration with time in Figure 4. The color contour indicates the distribution of the longitudinal field (B_x) while the strength of the azimuthal field (B_ϕ) is overplotted with solid lines. In Figure 5, we plot the x -component of the vorticity vector (ω_x), where

$$\omega_x = \frac{\partial V_z}{\partial y} - \frac{\partial V_y}{\partial z}, \quad (18)$$

and white and black colors indicate positive (counter-clockwise) and negative vorticity (clockwise), respectively. These figures (Figures 4 and 5) look similar to those of previous experiments within the convection zone (Moreno-Insertis & Emonet 1996; Emonet & Moreno-Insertis 1998). Figures 4(a) and 5(a) present the initial state: the flux tube has a circular shape and there is no vorticity within the domain. As the tube begins to emerge, the field strength reduces and the tube expands, since the background density

decreases with height (Figures 4(b)-(d)). Also, the external flow from the apex to the flanks of the tube creates negative and positive vortex sheets in the right and left side of the main tube, respectively (Figures 5(b)-(d)). Therefore, the tube is deformed and the wake behind the main tube grows with a pair of counter-rotating vortex rolls. Because of the azimuthal fields, however, the tube is not entirely fragmented into an “umbrella shape.” As a consequence, the rising tube feels aerodynamic drag, and, thus, the rise velocity levels off at this time. The longitudinal field component keeps its strength in the core of the vortex rolls as well as in the main tube (see Figure 4(e)). Behind the main tube, in $-100 < z/H_0 < -60$ in Figure 4(f), there is a weakly magnetized tail with non-zero vorticity (Figure 5(f)).

During this phase, the rise speed of the tube center reveals oscillation as seen in Figure 3(b). This is a result of torsional oscillation due to the differential buoyancy caused by the magnetic field distribution (e.g. Moreno-Insertis & Emonet 1996). Initially, the flux tube has its maximum field strength at the center and thus the central region rises faster than the periphery. Therefore, the azimuthal field around the apex is compressed and strengthened to fortify the magnetic tension force, which inhibits the tube from a distortion into vortex rolls. The tension force decelerates the center of the tube and, as a result, induces the internal torsional oscillation. The period of this oscillation is observed to be consistent with the time of the azimuthal Alfvén speed traveling across the tube’s diameter.

At around $t/\tau_0 = 500$, the rise motion begins to decelerate and the front of the tube expands horizontally, since the tube is close enough to the surface. The plasma above the rising tube cannot move through the isothermal (i.e., convectively stable) photosphere so that the fluid is compressed and piles up between the front of the tube and the photosphere. The fluid between them suppresses the rising motion of the flux below, and thus, the flux extends sideways. The horizontal expansion caused by the photosphere was

previously reported by Magara (2001). His flux tube was not so deformed as to develop a wake including vortex rolls and directly entered the photosphere mostly keeping its original cylindrical shape, because the initial tube was located just beneath the surface ($z_{\text{tube}} = -1800$ km) with a strong field strength ($B_{\text{tube}} = 7760$ G). In our case, the initial tube was embedded so deep in the convection zone ($z_{\text{tube}} = -20,000$ km) that the wake behind the main tube was formed and the drag force became more effective. The velocity shear between the horizontal flow above the tube and the photosphere forms vortex sheets at around $z/H_0 \sim 0$ (Figure 5(e); the positive sheet in the right half, and the negative in the left). Finally, at $t/\tau_0 = 700$, the flux tube has a ∇ -shaped structure and the magnetic field extends widely beneath the surface (Figure 4(f)). The vortex sheet at the tube front collides against the subphotospheric sheet (Figure 5(f)). In this stage, the azimuthal field beneath the surface is much stronger than the longitudinal field because of the radial expansion of the flux tube (Parker 1974, 1979).

3.2. Comparison with an Analytic Model

Fan et al. (1998) compared their numerical results of the emerging twisted flux tube obtained by 2.5D anelastic MHD experiments with those of the thin-flux-tube model. According to Fan et al. (1998), the motion of the cylindrical flux tube rising by its magnetic buoyancy is described as

$$I\rho\frac{dV_z}{dt} = -\Delta\rho g - C_D\frac{\rho|V_z|V_z}{\pi R}, \quad (19)$$

where I is the enhanced inertia factor (~ 2), C_D is the drag co-efficient of order unity, and $\Delta\rho = \rho_i - \rho$ is the density difference between the flux tube (ρ_i) and the external medium (ρ). From Equation (19), one can calculate the rising velocity of the tube $V_z(t)$ and the height of the tube center $z(t)$. We consider the effect of the mass pile-up between the flux

tube and the photosphere and replace $\Delta\rho$ with an additional effect as

$$\begin{aligned}\Delta\rho' &= \Delta\rho + F\Delta\rho_{\text{acm}} \\ &= \rho_i - \rho + F[\bar{\rho}_{\text{acm}}(0) - \bar{\rho}_{\text{acm}}(t)] .\end{aligned}\quad (20)$$

Here,

$$\bar{\rho}_{\text{acm}}(0) = \frac{1}{z_{\text{ph}} - z(0)} \int_{z(0)}^{z_{\text{ph}}} \rho_s(\zeta) d\zeta \quad (21)$$

is the plasma on the flux tube in the initial state ($z_{\text{ph}} = 0$, $z(0) = z_{\text{tube}} = -100H_0$, and $\rho_s(z)$ is given by Equation (11)), and

$$\bar{\rho}_{\text{acm}}(t) = \frac{1}{z_{\text{ph}} - z(t)} \int_{z(t)}^{z_{\text{ph}}} \rho_s(\zeta) d\zeta \quad (22)$$

is the background plasma at a given time. That is, $\Delta\rho_{\text{acm}} = \bar{\rho}_{\text{acm}}(0) - \bar{\rho}_{\text{acm}}(t)$ corresponds to a density that would have been accumulated by an ideal rising sheet extending horizontally. To consider the effect of the tube's shape and the draining of the plasma from the apex, we multiply it by a factor $F(< 1)$, which depends on the field geometry and its initial depth from the surface (R_{tube} and z_{tube}). In the present study, we vary F to fit the analytic model to the obtained data and assume it as a constant. The relation between F and R_{tube} and z_{tube} requires much work, which we shall leave for future research. Applying $\Delta\rho'$ and dividing Equation (19) by ρ , we get

$$I \frac{dV_z}{dt} = -\frac{\Delta\rho'}{\rho} g - \frac{C_D}{\pi R} |V_z| V_z . \quad (23)$$

If pressure balance, mass and flux conservation, and adiabatic evolution are assumed, the buoyancy and the radius of the model tube can be defined as

$$-\frac{\Delta\rho'}{\rho} g = \left(-\frac{\Delta\rho}{\rho} g\right)_{z=z_{\text{tube}}} \left[\frac{(\Gamma + 1) - z/H_0}{(\Gamma + 1) - z_{\text{tube}}/H_0} \right]^{\Gamma-1} + F \frac{\Delta\rho_{\text{acm}}}{\rho} , \quad (24)$$

$$R(z) = R(z = z_{\text{tube}}) \left[\frac{(\Gamma + 1) - z/H_0}{(\Gamma + 1) - z_{\text{tube}}/H_0} \right]^{\Gamma/2} , \quad (25)$$

where $\Gamma = 1/(\gamma - 1)$. Here we use their initial values obtained as

$$\left(-\frac{\Delta\rho}{\rho}g\right)_{z=z_{\text{tube}}} = \frac{\iint (-\Delta\rho/\rho)g B_x dydz}{\iint B_x dydz}, \quad (26)$$

and

$$R(z = z_{\text{tube}}) = \left[\frac{\iint [(y - y_{\text{tube}})^2 + (z - z_{\text{tube}})^2] B_x dydz}{\iint B_x dydz} \right]^{1/2} \quad (27)$$

(see Fan et al. 1998). We can calculate the time evolution of the model tube by integrating Equation (23).

In Figure 6(a), the variation of the rise speed at the tube center is presented in comparison with the analytic model (the dotted line is for the model by Fan et al. (1998) using $\Delta\rho$ and the solid line for our model using $\Delta\rho'$), while the heights of the tube centers of the numerical and the analytic model are indicated in Figure 6(b). We use $C_D = 2.0$ and $F = 0.001$. In Figure 6(a), the solid curve levels off after $t/\tau_0 = 100$. This means that the wake develops from this time and the drag force becomes more efficient. Parker (1975) analytically calculated the terminal velocity of the rising. Considering Equation (19) = 0 and using Equations (26) and (27), the terminal velocity can be obtained as

$$V_{z \text{ term}} = \left[-\frac{\Delta\rho}{\rho}g \frac{\pi R}{C_D} \right]^{1/2} = 0.14 C_{s0}, \quad (28)$$

which is rather a good estimation. In the earlier phase ($t/\tau_0 < 400$), the torsional oscillation due to the differential buoyancy is seen in Figure 6(a), which was mentioned in §3.1.

After $t/\tau_0 = 500$, the rising flux tube decelerates as the mass on the tube is compressed and piles up, since the mass cannot persist through the convectively stable surface. This deceleration indicates that, before $t/\tau_0 = 500$, the cross-sectional evolution as a whole can be regarded as radial, although the tube suffers aerodynamic deformation; after that time, however, the mass pile-up becomes much more efficient so that the tube decelerates and the apex expands horizontally to become ∇ -shaped (see the solid and the dotted line in Figure 6(a)).

Figure 7(a) shows the density accumulation $[\rho(t) - \rho_s]/\rho_0$, where ρ_s is the initial background density profile (see Equation (11)), and the field lines with velocity vectors at the time $t/\tau_0 = 600$. It reveals that, because of the relative mass draining from the apex of the tube to the flanks, the density piles up in front of the rising tube around $(y/H_0, z/H_0) = (0, -12)$ to form a boundary layer with a finite width ($\sim 40H_0$). In the imaginary sheet case, however, the fluid would pile up on the rising sheet as a boundary layer with an infinite width, since there is no draining (see Paper I). Therefore, the factor F (the ratio of the actual accumulation to the imaginary one) becomes relatively small.

To show that the contribution of ram pressure to the pressure excess (which is related to density excess) at the tube front is small enough, in Figure 7(b) we plot vertical distributions of ram pressure $\rho(t)\Delta V_z^2(t)/p_0$, where $\Delta V_z(t) = V_z(t) - V_z(t, z = -14H_0)$ is the flow velocity relative to the rising tube, pressure excess $[p(t) - p_s]/p_0$, and the total field strength $|B|/B_0$ at $t/\tau_0 = 600$ along the symmetric axis $y/H_0 = 0$. In front of the rising tube ($z/H_0 = -12$), pressure excess reveals a hump $\Delta P/p_0$, which is indicated by an arrow in the middle of Figure 7(b). The corresponding ram pressure $\rho(t)\Delta V_z^2(t)/p_0$ is also indicated with arrows in the bottom of the figure. From this figure, we can see that the effect of the ram pressure $\rho(t)\Delta V_z^2(t)/p_0 \sim 0.002$ is much smaller than the hump of the pressure excess $\Delta P/p_0 \sim 1$. That is, the contribution of the ram pressure to the density accumulation in front of the tube is negligible.

From Figure 7(a), we can estimate the order of F . The actual mass pile-up along the symmetric axis $y/H_0 = 0$ is

$$\begin{aligned} \Delta\rho_{\text{sim}} &= \frac{1}{z_{\text{ph}} - z_{\text{apex}}(600\tau_0)} \int_{z_{\text{apex}}(600\tau_0)}^{z_{\text{ph}}} [\rho(600\tau_0) - \rho_s] d\zeta \\ &= 0.73\rho_0, \end{aligned} \tag{29}$$

where $z_{\text{apex}}(600\tau_0) = -12H_0$ is the height of the apex of the tube at $t = 600\tau_0$ (see Figure 7). On the other hand, the density enhancement in front of the imaginary emerging sheet

at this time can be estimated from the background profile $\rho_s(z)$ as

$$\begin{aligned} \Delta\rho_{\text{acm}} &= \bar{\rho}_{\text{acm}}(0) - \bar{\rho}_{\text{acm}}(600\tau_0) \\ &= \frac{1}{z_{\text{ph}} - z(0)} \int_{z(0)}^{z_{\text{ph}}} \rho_s(\zeta) d\zeta - \frac{1}{z_{\text{ph}} - z(600\tau_0)} \int_{z(600\tau_0)}^{z_{\text{ph}}} \rho_s(\zeta) d\zeta \\ &= 96.1\rho_0, \end{aligned} \tag{30}$$

where $z(600\tau_0) = -25H_0$ is the height of the tube's center at $t = 600\tau_0$ (see Figure 6(b)).

Therefore, we can see that the order of the factor F is

$$F = \frac{\Delta\rho_{\text{sim}}}{\Delta\rho_{\text{acm}}} = \frac{0.73\rho_0}{96.1\rho_0} = 0.007 = O(10^{-2}). \tag{31}$$

Here, we consider the density accumulation only along the axis $y/H_0 = 0$ in Equation (29). The factor F would be of order 10^{-3} if we take it into account that the accumulation in the neighboring region is less than that along $y/H_0 = 0$ due to mass draining.

By varying F to fit the analytic model to the obtained data and plotting the density pile-up in the interior, we can conclude that the deceleration of the tube is caused by the accumulation of the plasma ahead of the tube. Fan et al. (1998) and Cheung et al. (2006) also reported this deceleration. However, their calculations did not include the convectively stable photosphere but assumed the non-penetrating or closed top boundaries, which are reasonable approximations for the photosphere compared to our simulation.

3.3. Further Evolution to the Corona

After $t/\tau_0 = 800$, the second-step emergence from the surface to the corona occurs due to the magnetic buoyancy instability (Figures 2(f)-(i)). Figure 8(a) shows the vertical distribution of magnetic and gas pressure, and density along the symmetric axis $y/H_0 = 0$ at $t/\tau_0 = 800$, i.e., just before the secondary evolution starts. As can be seen from this figure, the site of the second-step evolution has a top heavy structure, and there is a relative

“pressure hill,” which is consistent with preceding studies (Magara 2001; Archontis et al. 2004).

To confirm that further evolution is caused by the magnetic buoyancy instability, we conduct the same analysis as in Paper I. Newcomb (1961) revealed the criterion for the magnetic buoyancy instability of a flat magnetized atmosphere is

$$-\frac{\partial\rho}{\partial z} < \frac{\rho^2 g_0}{\gamma p} . \quad (32)$$

From this relation, we define the index

$$\psi = -\frac{\partial\rho}{\partial z} - \frac{\rho^2 g_0}{\gamma p} , \quad (33)$$

where the area with negative ψ is magnetic buoyancy-unstable. We show the ψ distribution in Figure 8(b). As can be seen from Figure 8(b), the site of the second-step emergence ($y/H_0 = z/H_0 = 0$) is $\psi < 0$, i.e., the criterion (32) for the instability is satisfied. Thus, we can conclude that the further evolution to the corona occurs because of the magnetic buoyancy instability. At this site, the magnetic field intensity amounts to ~ 1 kG, and the plasma beta is $\beta \sim 2$.

In the upper atmosphere above the surface, the azimuthal component of the magnetic field is very dominant. The second-step nonlinear evolution develops in a self-similar way; the expansion law was given by Shibata et al. (1989). It can be described as follows:

$$V_z/C_{s0} = az/H_0 , \quad (34)$$

$$\rho \propto z^{-4} , \quad (35)$$

and

$$|B_y| \propto z^{-1} , \quad (36)$$

where $a \sim 0.05$ when plasma- β is $0.5 - 2.0$. The above relations are plotted in Figure 9 for $t/\tau_0 = 850, 870, \text{ and } 890$. In Figure 9(a), we use $a = 0.04$, which is appropriate because plasma- β was ~ 2 at the point of the further evolution ($z \sim 0$ at the time $t/\tau_0 = 800$).

In the final phase, at $t/\tau_0 = 980$, the coronal loop is formed with $400H_0 = 80,000$ km in width and $200H_0 = 40,000$ km in height (see Figure 2(i)). The size of the loop is similar to that of the case with a flux sheet (Paper I). The photospheric field strength is $400 - 700$ G at this time.

4. Dependence on the Initial Twist and the Field Strength

We carry out five additional calculations to investigate the dependence of the tube’s evolution on the twist and the field strength. These runs are summarized in Table 1. Parametric surveys on the twist and the field strength have done by Moreno-Insertis & Emonet (1996), Emonet & Moreno-Insertis (1998), Magara (2001), Murray et al. (2006), Murray & Hood (2008), and Toriumi et al. (2011). They found that the tube rises faster as the twist and the field becomes stronger.

Figure 10 shows the result of the parameter survey on the tube twist. In this figure, height-time relations of the tube tops are shown. In cases of a weaker twist ($q = 0.01/H_0$ and $0.05/H_0$), the flux tube shows “failed emergence.” That is, the rising flux cannot pass through the photosphere. The criterion for this failure is $q \lesssim 0.05/H_0$. In Paper I, we found that, when the initial field strength or the total magnetic flux is too weak, the resulting development also reveals “failed” evolution. Figure 11 shows the flux tubes with different initial twist when each tube center reaches $z/H_0 = -50$. From left to right, the twist parameter decreases. The upper panels present the flow field relative to the tube apex, $\mathbf{V}_{\text{rel}} = \mathbf{V} - \mathbf{V}_{\text{apex}}$, and the corresponding equipartition line. The equipartition line indicates

the tube boundary where the kinetic energy density of the relative flow $e_{\text{kin}} = \rho V_{\text{rel}}^2/2$ equals the energy density of the azimuthal field $e_{\text{mag}} = B_\phi^2/(8\pi)$. The lower panels show the longitudinal field strength B_x and the flow field \mathbf{V} . As can be seen from Figure 11, with a decreasing twist, the main tube is deformed by the external flow and the wake develops. In cases of a weaker twist, the counter-rotating vortices contain a large portion of the magnetic flux. Thus, when the tube reaches the surface, the apex of the tube cannot hold sufficient flux for the further evolution, which leads to “failed emergence.” The situation can also be explained as follows; when the initial twist is weak, the flux tube expands and extends very widely beneath the surface. Thus, the magnetic buoyancy falls short of compressing the flux to satisfy the criterion (32) for the second-step emergence. In Figure 12, we show the distribution near the surface for the case $q = 0.05/H_0$ at the time $t/\tau_0 = 1000$. Figure 12(a) plots the magnetic pressure, the gas pressure, and the density along the symmetric axis $y/H_0 = 0$. The subsurface magnetic field is not fortified enough so that the magnetic pressure is much smaller than the plasma pressure. Therefore, the index ψ (see §3.3) is not negative in almost the whole area shown in Figure 12(b), which means that the further evolution to the solar corona due to the magnetic buoyancy instability does not take place in this weaker twist case.

Figure 13 shows the height-time relations for the cases with $B_{\text{tube}} = 67B_0$, $50B_0$, and $33B_0$, which are indicated with dashed, solid, and dash-dotted lines. We can conclude from this figure that the rise speed is faster with the stronger field. As is the case with the dependence on the twist, we can say that, if the initial field is too weak, the rise speed is slower and the flux tube cannot pass through the surface to rise further into the corona. The general tendency of the parametric studies varying the tube’s twist and the strength is consistent with previous two- and three-dimensional experiments (Moreno-Insertis & Emonet 1996; Emonet & Moreno-Insertis 1998; Magara 2001; Murray et al. 2006; Murray & Hood 2008; Toriumi et al. 2011).

5. Summary and Discussion

The numerical experiments studied in this paper are on the cross-sectional evolution of the emerging twisted flux tube. In this section, we summarize the calculations presented above and discuss the results. The discussions are mainly in connection with Paper I. We can predict the conditions for three-dimensional experiments by considering the results of the present and previous two-dimensional studies. So, in this section, we discuss the two-dimensional results in connection with our future three-dimensional experiments.

In this paper, we have studied the dynamical evolution of the twisted flux tube that emerged from the deep convection zone. For the typical case, the initial flux tube is located at $z = -100H_0 = -20,000$ km with the axial field strength $B_{\text{tube}} = 50B_0 = 1.5 \times 10^4$ G, the tube radius $R_{\text{tube}} = 5H_0 = 1000$ km, and the total magnetic flux $\Phi = 4.7 \times 10^{20}$ Mx. The tube is initially buoyant and, thus, begins to rise through the convection zone. Halfway to the surface, after $t = 100\tau_0 = 2500$ s, the periphery of the tube is peeled away to develop a wake, composed of vortex rolls and a long-drawn tail, due to the external flow from the apex to the flanks. As a result, the aerodynamic drag becomes more effective. However, the azimuthal field prevents the flux tube from being fragmented into a pair of counter-rotating vortices moving away from each other, so that the expansion as a whole can be said to be radial. The picture of the emergence within the convective layer is similar to previous papers (e.g. Moreno-Insertis & Emonet 1996).

The essential difference from these preceding studies is the effect of the convectively stable photosphere; the apex of the tube expanding horizontally and the rising motion turning into the deceleration after $t = 500\tau_0 = 1.3 \times 10^4$ s, because the rising tube comes close to the photosphere. The deceleration occurs at ten times deeper than previously reported by Magara (2001); the deceleration depth is ~ -500 km in Magara’s case, while it is ~ -5000 km in our case, which shows that the flux tube slows down before the tube itself

reaches the surface. There seems to be another mechanism for the slowdown other than the tube itself entering the photosphere. The plasma on the flux tube piles up between the flux and the convectively stable surface, and depresses the flux below. We confirmed this effect by comparing the numerical result with an extended analytic model (see Section 3.2). As a result, the ∇ -shaped emerging flux extends widely beneath the surface ($\sim 40,000$ km in width). In this stage, the azimuthal field component is dominant, since the twist of the flux tube increases as the tube rises. When the horizontal flux at the photosphere becomes unstable to the magnetic buoyancy instability at $t = 800\tau_0 = 2.0 \times 10^4$ s, the second-step emergence to the corona takes place (“two-step emergence”). The evolution above the surface is similar to that of Magara (2001). The nonlinear evolution is well described by the expansion law given by Shibata et al. (1989). The consequent coronal loop at $t = 980\tau_0 = 2.5 \times 10^4$ s has its width $\sim 400H_0 = 80,000$ km and height $\sim 200H_0 = 40,000$ km, and the photospheric field is $(1.3 - 2.3)B_0 = 400 - 700$ G.

By performing parameter studies, we found that the initial twist necessary for the further evolution is $q > 0.05/H_0 = 2.5 \times 10^{-4} \text{ km}^{-1}$ when the axial field $B_{\text{tube}} = 50B_0 = 1.5 \times 10^4$ G. If q is less than this value, the emerging tube remains within the convection zone (“failed emergence”). We also found that the flux with a weaker field strength shows the failed emergence. When the tube twist is $q = 0.1/H_0 = 5.0 \times 10^{-4} \text{ km}^{-1}$, the flux with $B_{\text{tube}} = 33B_0 = 1.0 \times 10^4$ G cannot rise further above the surface.

In Paper I, we carried out numerical experiments on the two-dimensional undular evolution of the flux sheet from the deep convection zone ($z = -20,000$ km). We found that the emerging flux sheet also decelerates in the convection zone. However, deceleration depth is deeper than that of the present study. Table 2 summarizes the characteristic values of both types of emergence. As seen from Table 2, the initial conditions (the field strength, the total magnetic flux, the sheet thickness and the tube radius, and the depth) are similar

to each other, while the obtained values concerning the evolutions in the convection zone (the arrival time at the photosphere and the deceleration depth) are different. That is, the twisted flux tube rises faster than the flux sheet and the deceleration occurs at a higher altitude. The difference between the two cases comes from the geometry of the emerging fluxes, i.e., a sheet or a tube. The plasma on the emerging flux tube can flow around the tube’s cross-section so that the tube rises faster. The fluid on the flux sheet, however, drains only along the magnetic field lines to both troughs, so that the plasma suppresses and slows down the rising sheet below halfway to the surface. As for the twisted flux tube, the deceleration occurs in the later phase when the tube itself approaches the surface and begins to expand horizontally (see §3.1 and §3.2). It should be noted that, in the initial state, the flux sheet is in hydrostatic equilibrium while the flux tube is in mechanically non-equilibrium. In addition, the mass draining along the longitudinal field line is not considered in the present tube calculation. Three-dimensional experiments are required to investigate these effects.

By conducting the parameter survey, we found that the emerging flux tube cannot rise further if the initial twist is too weak (“failed” case), because the weak azimuthal field cannot hold the tube’s coherency and thus cannot hold the field intensity necessary for the second-step emergence. Such a flux remains below the surface and floats around the solar interior. The condition for the “two-step emerging” flux tube that yields a realistic active region at the surface is $B_{\text{tube}} \gtrsim 50B_0 = 1.5 \times 10^4 \text{ G}$ with $q \gtrsim 0.1/H_0 = 5.0 \times 10^{-4} \text{ km}^{-1}$ at $z = -100H_0 = -20,000 \text{ km}$. In Paper I, it was also found that there is a threshold of the flux sheet strength and the total flux for further emergence. That is to say, the emerging flux with a weak twist also shows “failed emergence” as well as the flux with a weak field strength and an insufficient total flux. If we put these results obtained from the two experiments together, the preferable initial conditions for the three-dimensional calculation using the twisted flux tube from the same depth ($z = -20,000 \text{ km}$) are the field

strength \sim a few 10^4 G, the total magnetic flux of $\sim 10^{21} - 10^{22}$ Mx, and sufficient twist ($q > 0.05/H_0 = 2.5 \times 10^{-4} \text{ km}^{-1}$). In future three-dimensional simulations, we will take into account the above mentioned conditions.

The comparison with the results by thin-flux-tube experiments (see §1) has been discussed in Paper I. In Figure 10 of Paper I, the typical case of the present calculation (Case 1 with 1.5×10^4 G and 4.7×10^{20} Mx) locates in the middle of the area for the two-step emergence. Moreno-Insertis et al. (1995) found that the magnetic flux tube with weaker field “explodes” within the interior and never reaches the surface; when the pressure gap between inside and outside the initial flux tube is too small, i.e., when the initial magnetic field is too weak, the tube will be collapsed at a certain height, since the pressure gap decreases. In Paper I, we found that the cases showing two-step emergence would have survived the “explosion” during their ascents through the interior. Therefore, we can see that the typical tube (the present Case 1) also would have emerged through the convection zone without suffering explosion.

Numerical computations were carried out on NEC SX-9 at the Center for Computational Astrophysics, CfCA, of the National Astronomical Observatory of Japan, and on M System (Fujitsu FX1) and V System (NEC SX-9) of JAXA Supercomputer System. The page charge of this paper is partly supported by CfCA. The authors thank Drs. H. Isobe and K. Shibata of Kyoto University and Dr. Y. Fan of the High Altitude Observatory, the National Center for Atmospheric Research. We are grateful to Mr. David Ward, the GCOE program instructor of the University of Tokyo for proofreading/editing assistance.

REFERENCES

- Abbett, W. P., & Fisher, G. H. 2003, *ApJ*, 582, 475
- Archontis, V., Moreno-Insertis, F., Galsgaard, K., Hood, A., & O’Shea, E. 2004, *A&A*, 426, 1047
- Caligari, P., Moreno-Insertis, F., & Schüssler, M. 1995, *ApJ*, 441, 886
- Cheung, M. C. M., Moreno-Insertis, F., & Schüssler, M. 2006, *A&A*, 451, 303
- Cheung, M. C. M., Schüssler, M., Moreno-Insertis, F. 2007, *A&A*, 467, 703
- Cheung, M. C. M., Schüssler, M., Tarbell, T. D., & Title, A. M. 2008, *ApJ*, 687, 1373
- Dorch, S. B. F., Archontis, V., & Nordlund, A. 1999, *A&A*, 352, L79
- Dorch, S. B. F. 2007, *A&A*, 461, 325
- D’Silva, S. & Choudhuri, A. R. 1993, *A&A*, 272, 621
- Emonet, T., & Moreno-Insertis, F. 1998, *ApJ*, 492, 804
- Fan, Y., Fisher, G. H., & Deluca, E. E. 1993, *ApJ*, 405, 390
- Fan, Y., Fisher, G. H., & McClymont, A. N. 1994, *ApJ*, 436, 907
- Fan, Y., Zweibel, E. G., & Lantz, S. R. 1998, *ApJ*, 493, 480
- Fan, Y. 2001, *ApJ*, 554, L111
- Galsgaard, K., Archontis, V., Moreno-Insertis, F., & Hood, A. W. 2007, *ApJ*, 666, 516
- Hood, A. W., Archontis, V., Galsgaard, K., & Moreno-Insertis, F. 2009, *A&A*, 503, 999
- Isobe, H., Miyagoshi, T., Shibata, K., & Yokoyama, T. 2005, *Nature*, 434, 478

- Longcope, D. W., Fisher, G. H., & Arendt, S. 1996, *ApJ*, 464, 999
- MacTaggart, D., & Hood, A. W. 2009, *A&A*, 507, 995
- Magara, T. 2001, *ApJ*, 549, 608
- Manchester, W., IV, Gombosi, T., DeZeeuw, D. & Fan, Y. 2004, *ApJ*, 610, 588
- Matsumoto, R., & Shibata, K. 1992, *PASJ*, 44, 167
- Moreno-Insertis, F., Caligari, P., & Schüssler, M. 1995, *ApJ*, 452, 894
- Moreno-Insertis, F., & Emonet, T. 1996, *ApJ*, 472, L53
- Moreno-Insertis, F. 2006, *ASP Conf. Ser.*, 354, 183
- Murray, M. J., Hood, A. W., Moreno-Insertis, F., Galsgaard, K., & Archontis, V. 2006, *A&A*, 460, 909
- Murray, M. J., & Hood, A. W. 2008, *A&A*, 479, 567
- Newcomb, W. A. 1961, *Phys. Fl.*, 4, 391
- Nozawa, S., Shibata, K., Matsumoto, R., Sterling, A. C., Tajima, T., Uchida, Y., Ferrari, A., & Rosner, R. 1992, *ApJS*, 78, 267
- Parker, E. N. 1955, *ApJ*, 121, 491
- Parker, E. N. 1974, *ApJ*, 191, 245
- Parker, E. N. 1975, *ApJ*, 198, 205
- Parker, E. N. 1979, *Cosmical magnetic fields: Their origin and their activity*
- Schüssler, M. 1979, *A&A*, 71, 79

Shibata, K., Tajima, T., Steinolfson, R. S., & Matsumoto, R. 1989, *ApJ*, 345, 584

Spruit, H. C. 1981, *A&A*, 98, 155

Toriumi, S. & Yokoyama, T. 2010, *ApJ*, 714, 505

Toriumi, S., Miyagoshi, T., Yokoyama, T., Isobe, H., & Shibata, K. 2011, *PASJ*, 63, 407

Tortosa-Andreu, A., & Moreno-Insertis, F. 2009, *A&A*, 507, 949

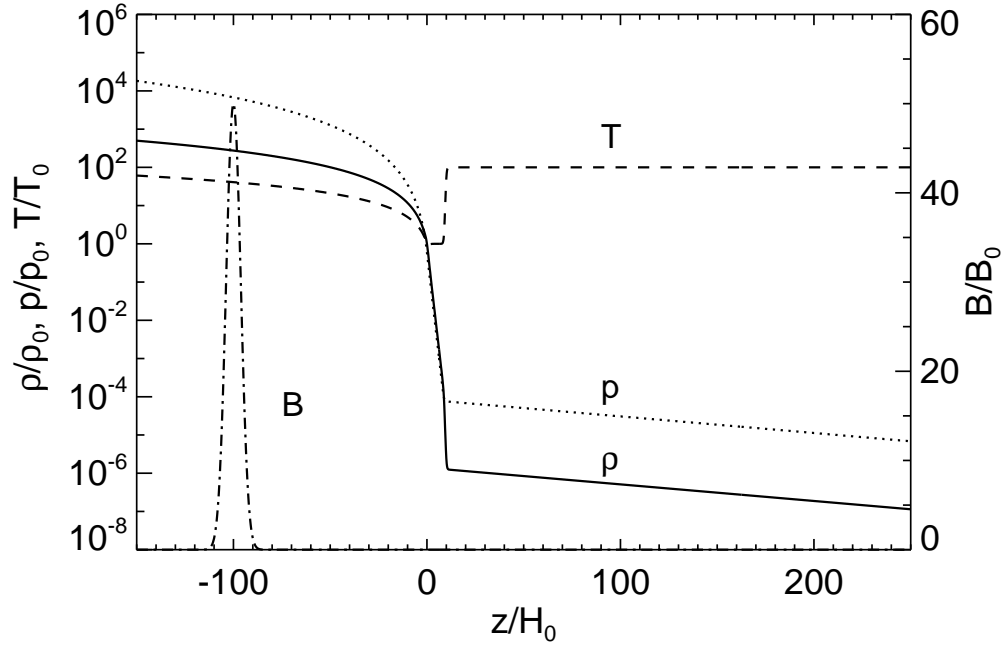


Fig. 1.— One-dimensional (z -)distributions of the initial background density (solid line), pressure (dotted line), and temperature (dashed line). The total magnetic field strength $B = [B_x^2 + B_\phi^2]^{1/2}$ of case 1 along the vertical axis $y = 0$ is overplotted with a dashed-dotted line.

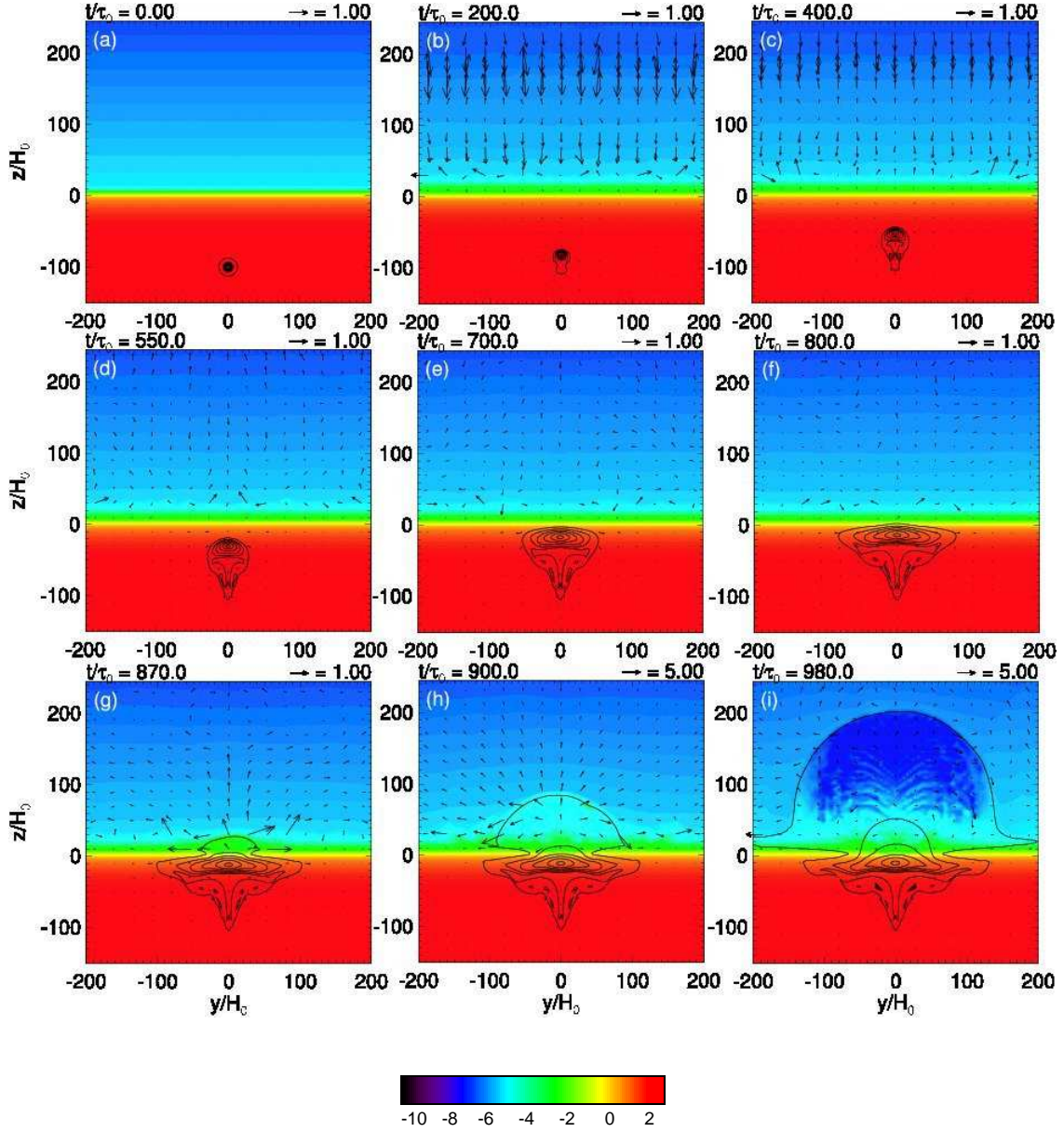


Fig. 2.— Time-evolution of the “two-step emergence” of the twisted flux tube (typical model). (a) $t/\tau_0 = 0$; (b) $t/\tau_0 = 200$; (c) $t/\tau_0 = 400$; (d) $t/\tau_0 = 550$; (e) $t/\tau_0 = 700$; (f) $t/\tau_0 = 800$; (g) $t/\tau_0 = 870$; (h) $t/\tau_0 = 900$; (i) $t/\tau_0 = 980$. Logarithmic density profiles ($\log_{10}(\rho/\rho_0)$) are indicated by color contours, while magnetic field lines and velocity vectors are overplotted with black lines and arrows, respectively. This figure is also available as an avi animation in the electronic edition of the *Astrophysical Journal*.

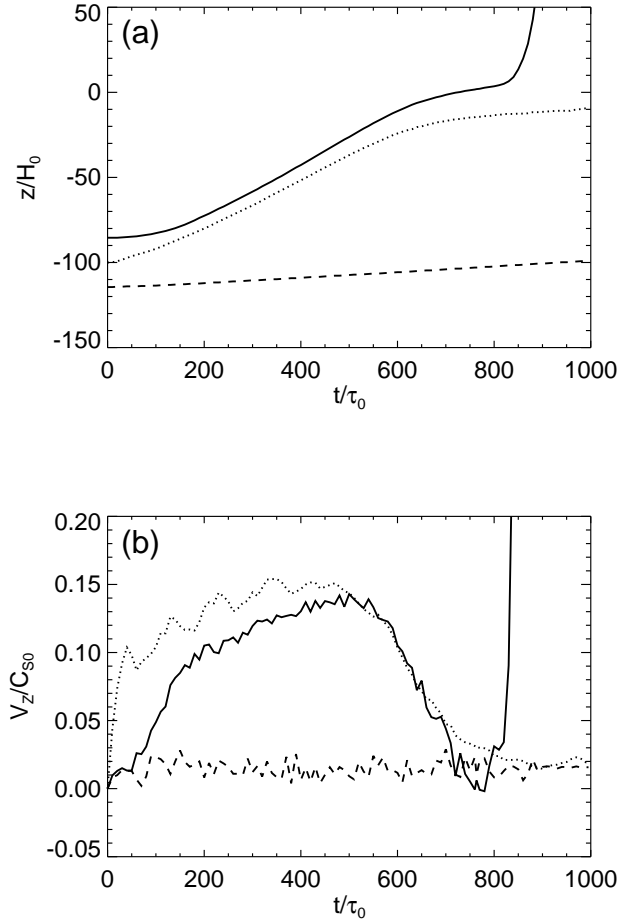


Fig. 3.— (a): Height-time relations at the top (solid line), the center (dotted line), and the bottom (dashed line) of the flux tube. (b): Gas velocities at these three points.

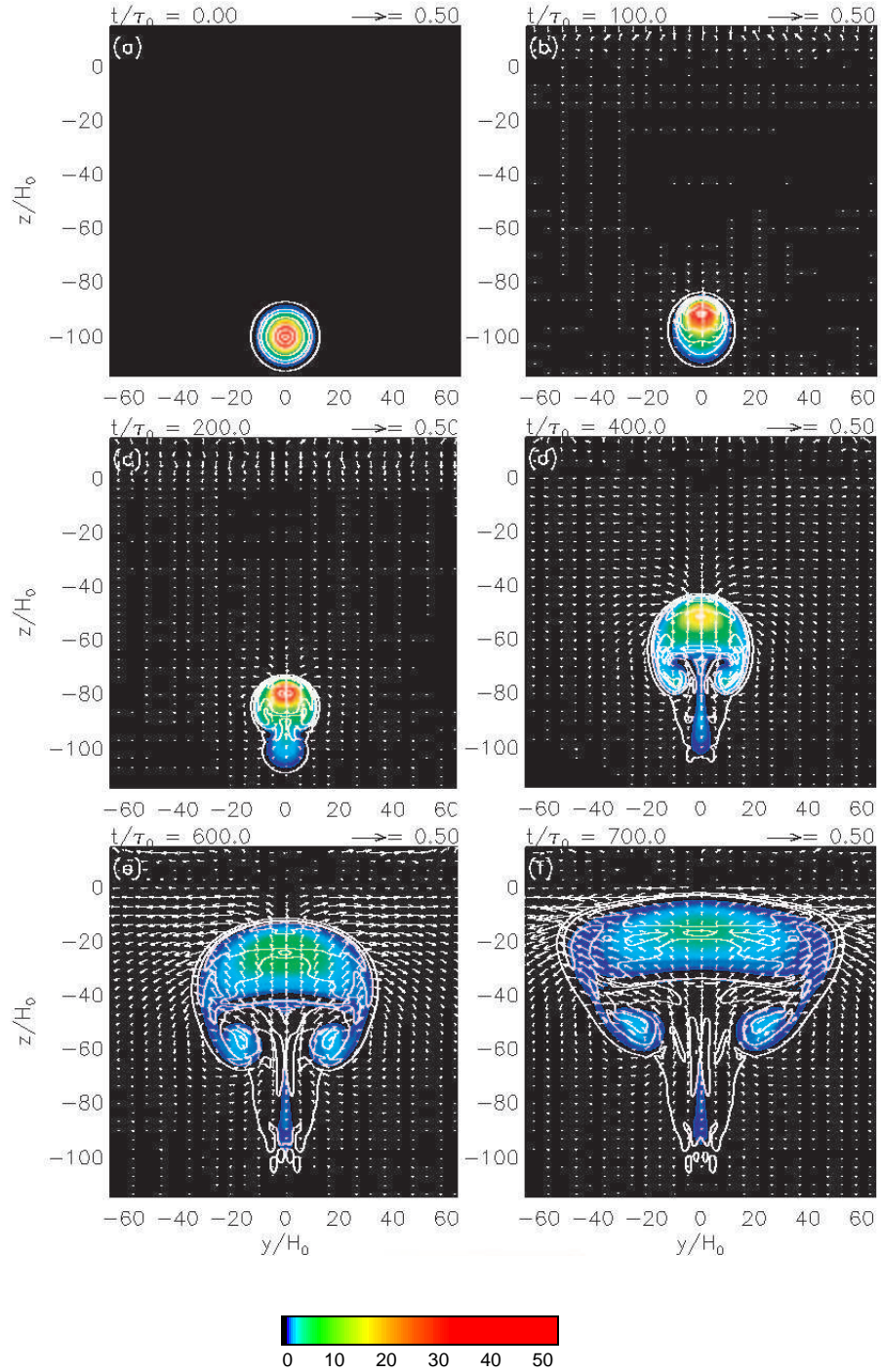


Fig. 4.— Time-evolution of the magnetic fields from $t/\tau_0 = 0$ to $t/\tau_0 = 700$. Color contour displays the longitudinal component B_x/B_0 , while the azimuthal component B_ϕ/B_0 is overplotted with solid lines.

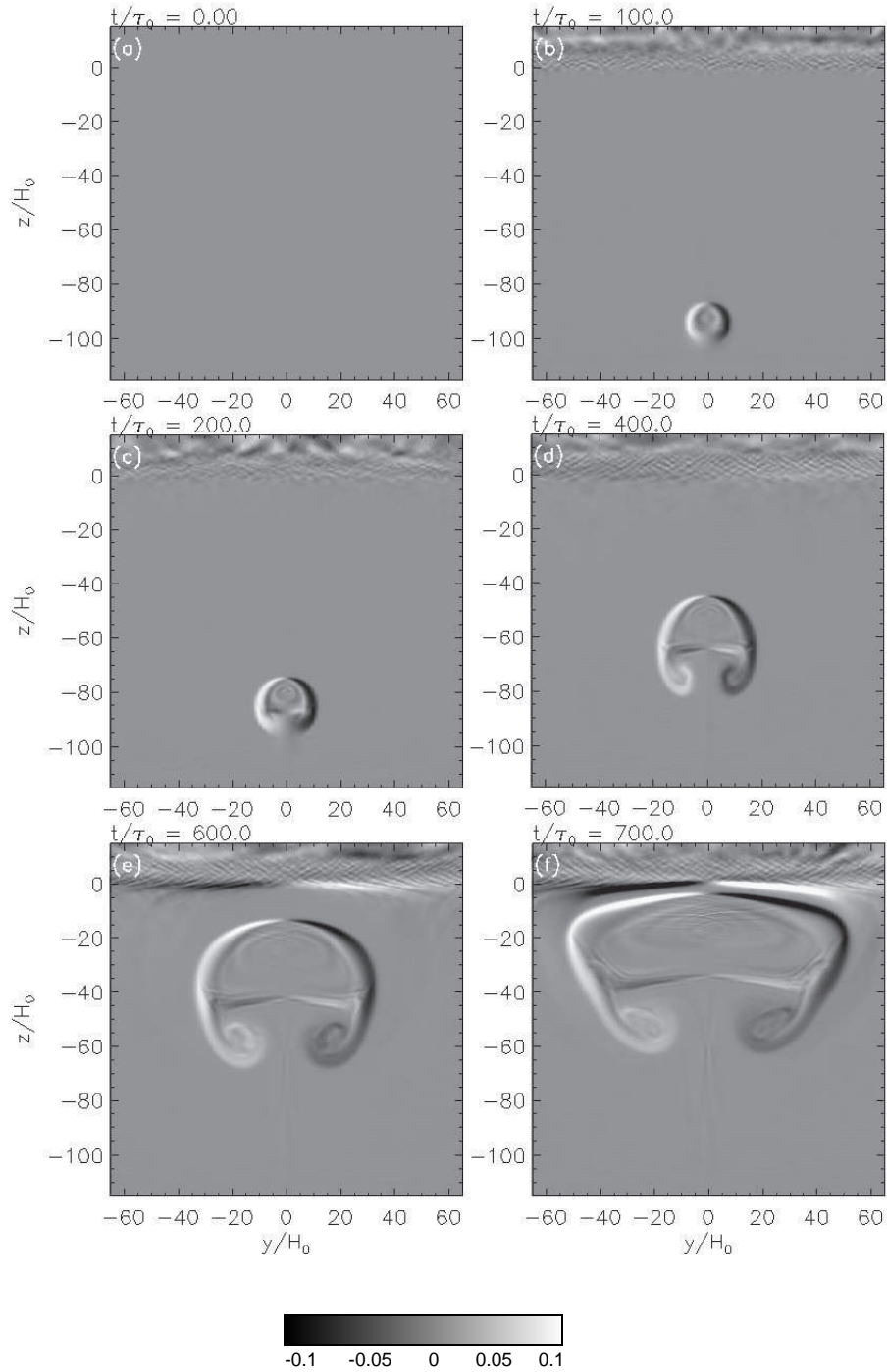


Fig. 5.— Same as Figure 4 but for the x -component of the vorticity. White indicates positive (counter-clockwise) vorticity, while black is negative (clockwise).

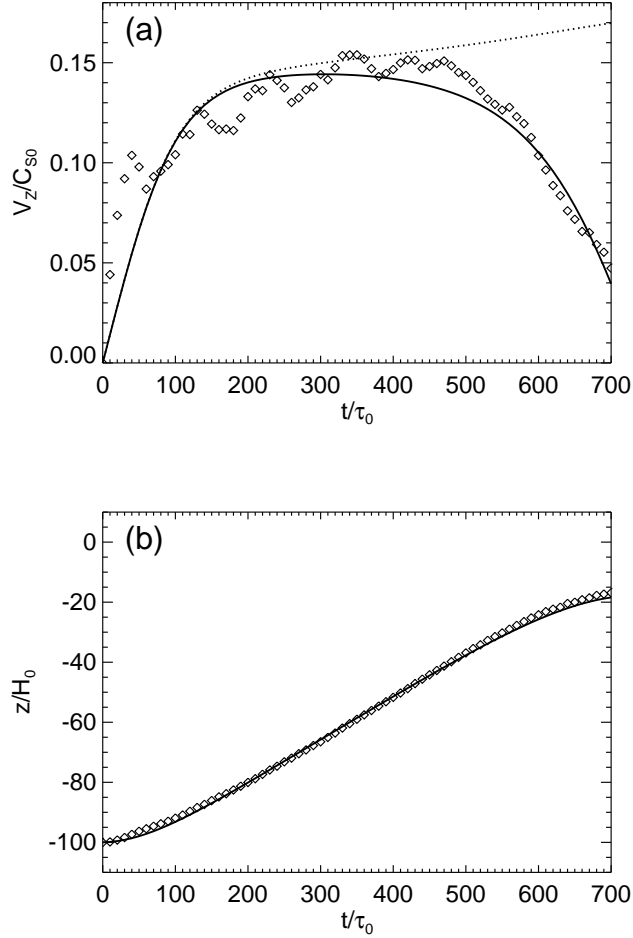


Fig. 6.— (a): The variation of rise velocity of the rising flux tube with time. Diamonds indicate the result of the numerical simulation. Solid line shows our analytic model, while dotted line represents the model by Fan et al. (1998). (b): Height-time relation of the numerical results (diamonds) and the analytic model (solid line). We use $C_D = 2.0$ and $F = 0.001$.

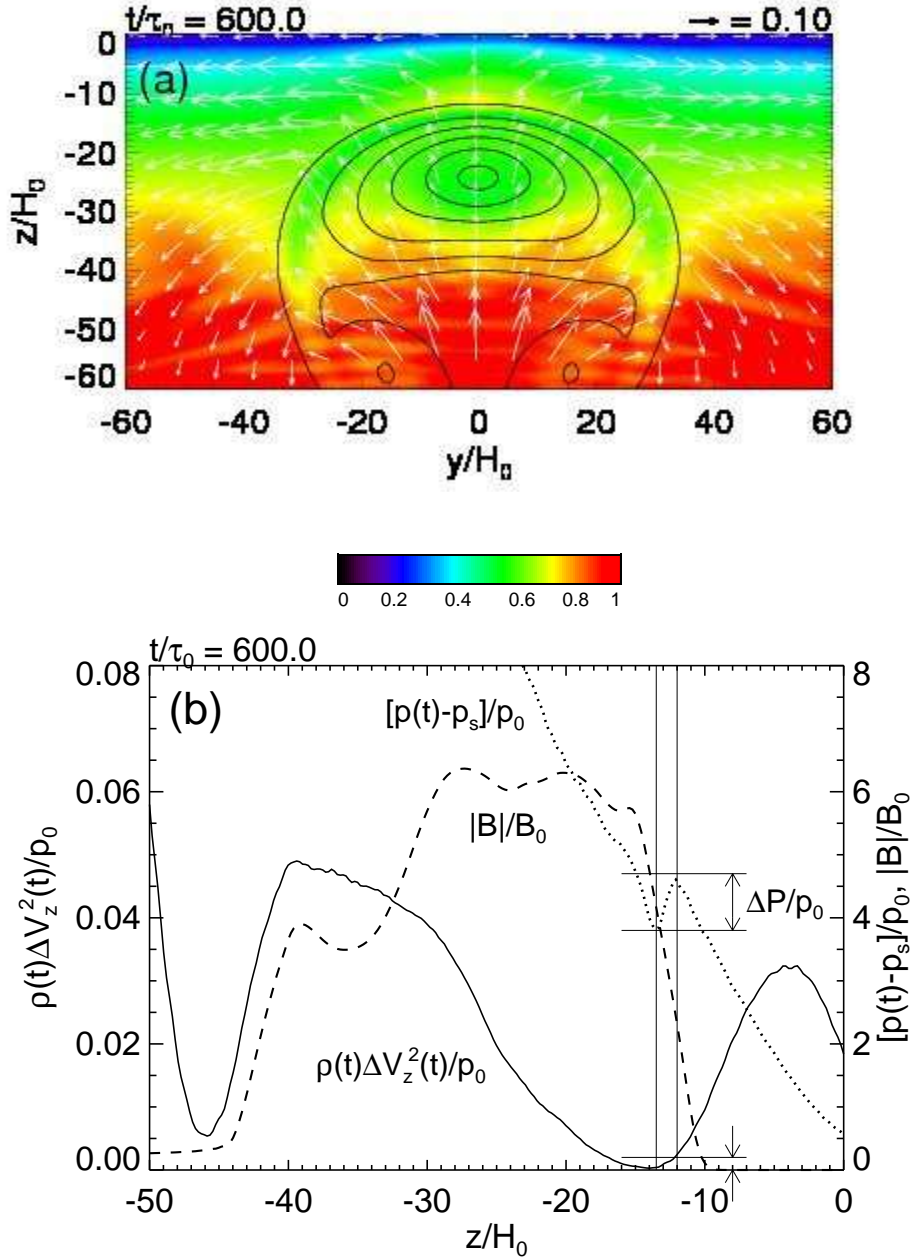


Fig. 7.— (a): The density accumulation $[\rho(t) - \rho_s]/\rho_0$, where ρ_s is the background density profile, and the field lines (contours) with velocity vectors (white arrows) at the time $t/\tau_0 = 600$ are shown. As the tube rises, the mass piles up in front of the flux tube around $(y/H_0, z/H_0) = (0, -12)$. (b): Vertical profiles of the ram pressure $\rho(t)\Delta V_z^2(t)/p_0$ (solid line), the pressure excess $[p(t) - p_s]/p_0$ (dotted line), and the total field strength $|B|/B_0$ (dashed line) along the symmetric axis $y/H_0 = 0$. The hump of the pressure excess $\Delta P/p_0$ is indicated by an arrow in the middle of the figure, while the corresponding ram pressure is indicated by arrows at the bottom (see text for details)

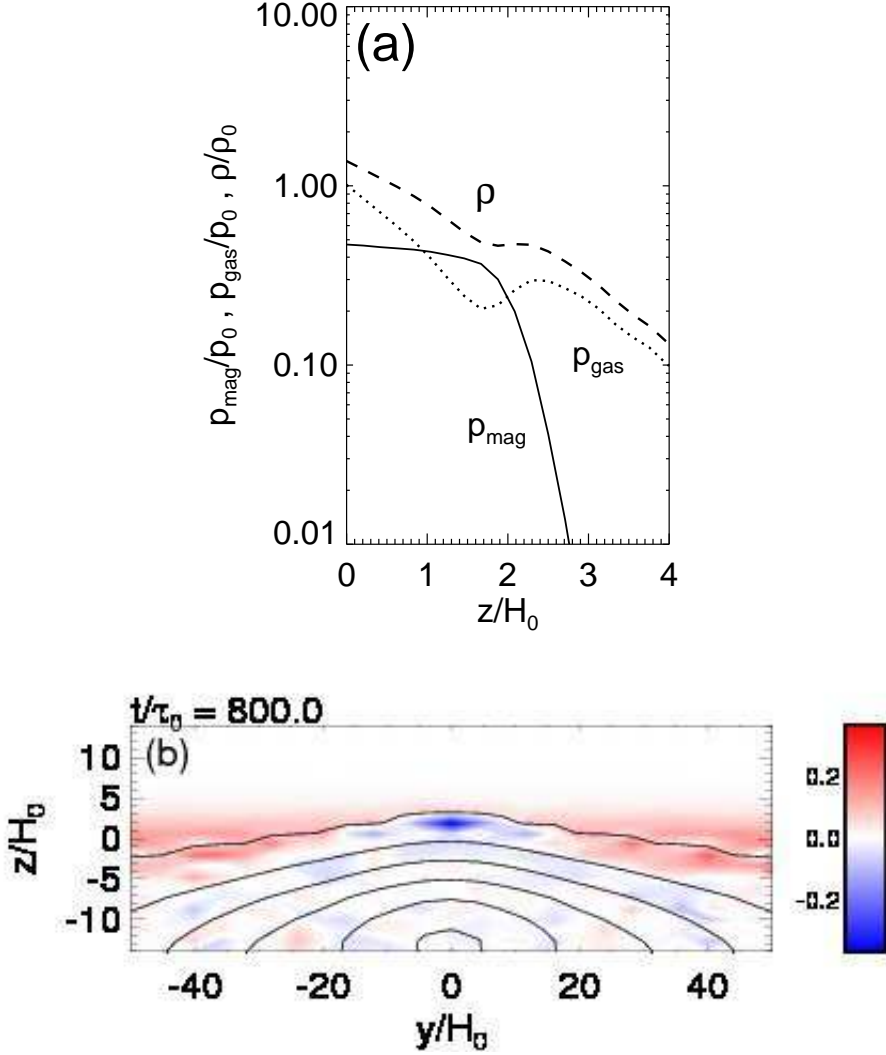


Fig. 8.— (a): Vertical distributions of the magnetic pressure (solid line), gas pressure (dotted line), and gas density (dashed line) along the axis $y/H_0 = 0$ at $t/\tau_0 = 800$. (b): Two-dimensional map of the index $\psi = -\partial\rho/\partial z - \rho^2 g_0/(\gamma p)$. Color contour indicates ψ , while azimuthal magnetic field lines are overplotted with solid lines. The area where index $\psi < 0$ is subject to the magnetic buoyancy instability.

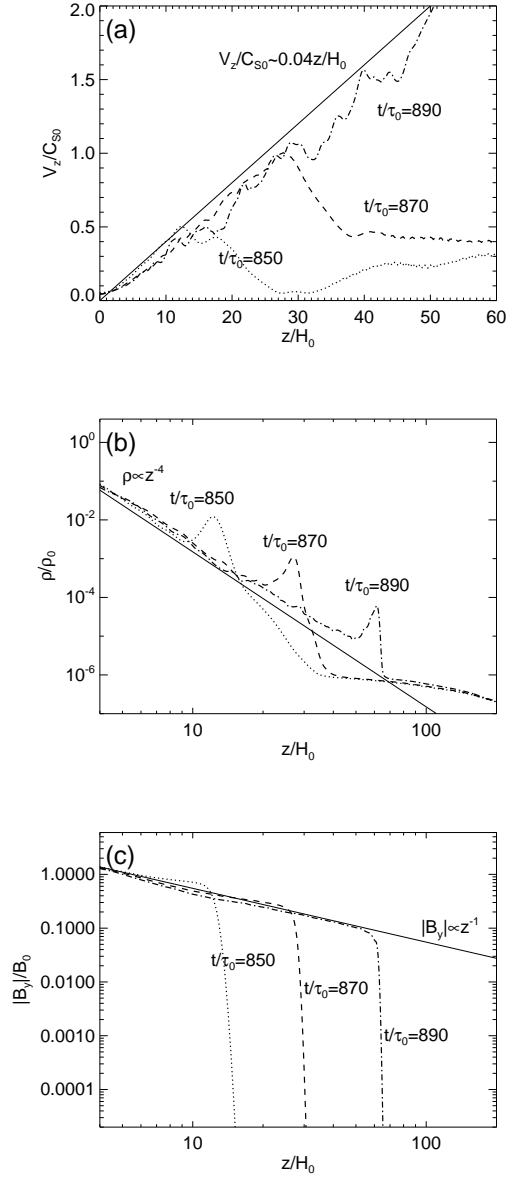


Fig. 9.— (a): Distribution of the upward velocity along the vertical axis $y/H_0 = 0$. Dotted, dashed, and dash-dotted lines indicate the distribution at $t/\tau_0 = 850$, 870, and 890, respectively. The solid line shows the theoretical velocity-height relation according to Shibata et al. (1989). (b): Distribution of the gas density. (c): Distribution of the horizontal component of the magnetic field.

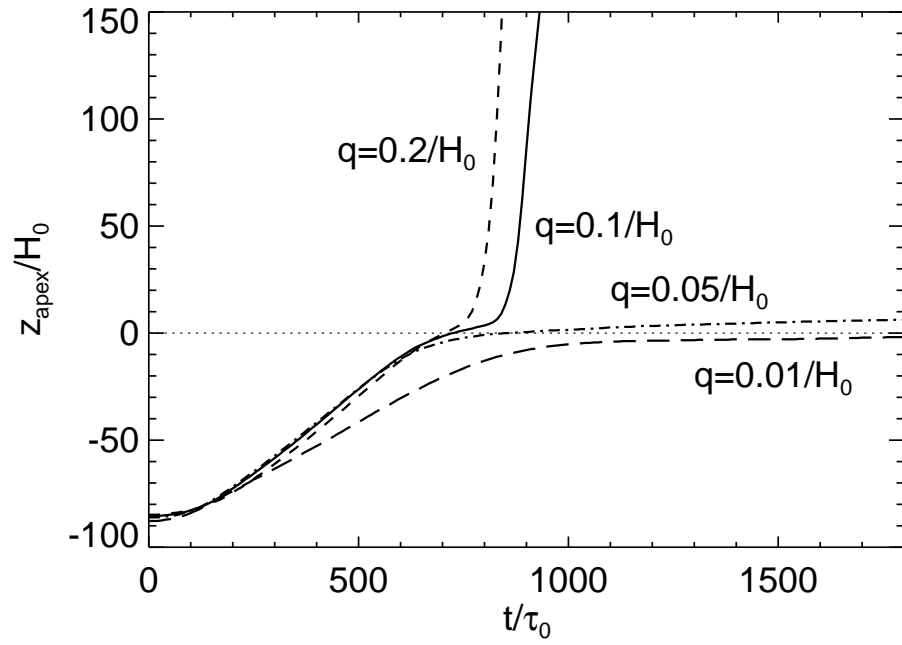


Fig. 10.— Height-time relation of the top of the flux tube. Dashed, solid, dash-dotted, and long dashed lines represent cases for $q = 0.2/H_0$, $0.1/H_0$, $0.05/H_0$, and $0.01/H_0$, respectively. Dotted line indicates the photospheric level.

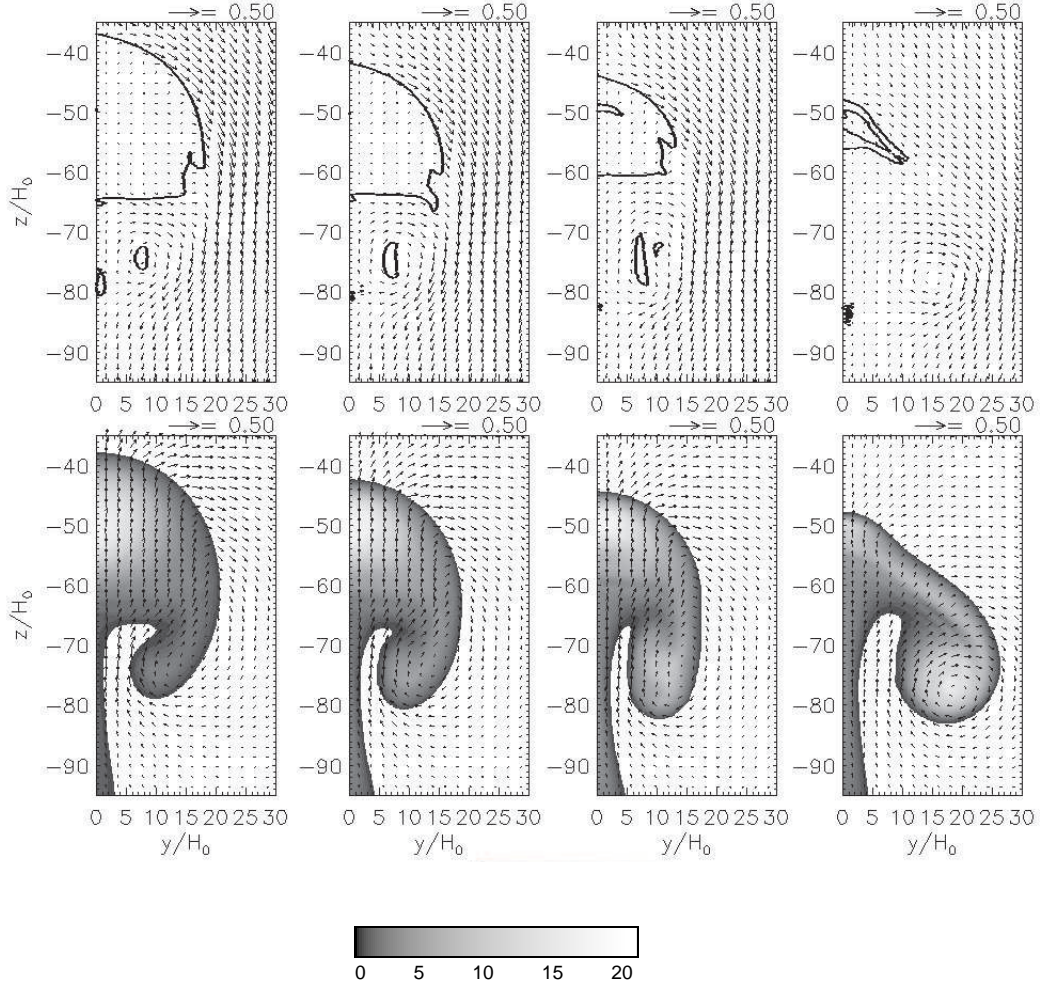


Fig. 11.— Cross-section of the flux tubes with different initial twist when their centers are at $z/H_0 = -50$. From left to right, the twist parameters and their corresponding times are $q = 0.2/H_0$, $0.1/H_0$, $0.05/H_0$, and $0.01/H_0$, and $t/\tau_0 = 460$, 410 , 390 , and 450 , respectively. *Top*: The velocity relative to the apex of the tube and the equipartition line (see text for details). *Bottom*: The longitudinal magnetic field strength and the flow fields.

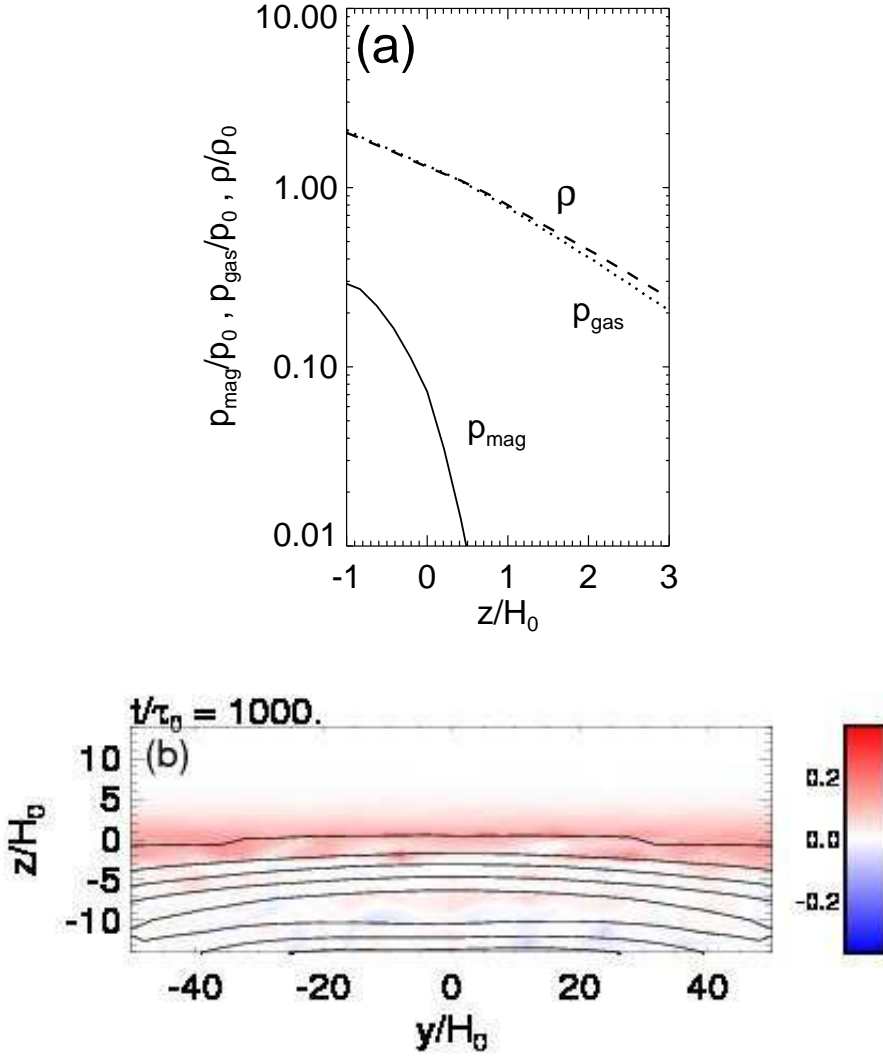


Fig. 12.— The plots for the case with $q = 0.05/H_0$ at $t/\tau_0 = 1000$. (a): Vertical distributions of the magnetic pressure (solid line), gas pressure (dotted line), and gas density (dashed line) along the axis $y/H_0 = 0$. (b): Two-dimensional map of the index ψ (see §3.3).

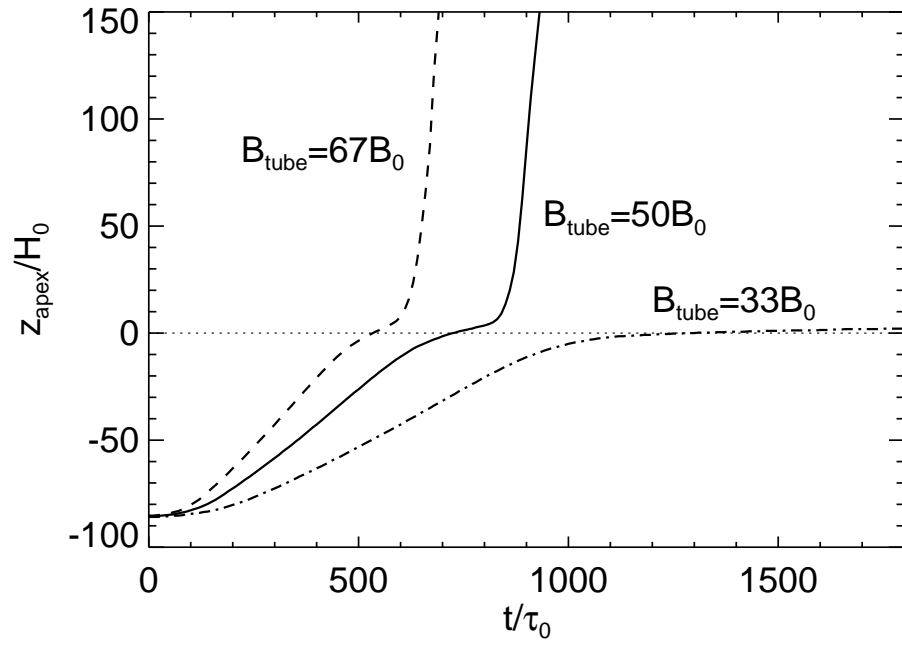


Fig. 13.— Height-time relation of the top of the flux tube. Dashed, solid, and dash-dotted lines represent cases for $B_{\text{tube}} = 67B_0$, $50B_0$, and $33B_0$, respectively. Dotted line indicates the photospheric level.

Table 1. Summary of Cases

Case	B_{tube} (300 G) ^a	R_{tube} (200 km) ^b	q (0.005 km ⁻¹) ^c
1	50	5	0.10
2	50	5	0.20
3	50	5	0.05
4	50	5	0.01
5	67	5	0.10
6	33	5	0.10

^aMagnetic field strength at the tube center.

^bTube radius.

^cTwist parameter.

Table 2. Comparison of the Two Types of the Flux Emergence

Characteristic Variables	Undular Emergence of a Flux Sheet ^a	Non-equilibrium Emergence of a Twisted Flux Tube ^b
Initial Field Strength	$1.0 \times 10^4 \text{G}$	$1.5 \times 10^4 \text{ G}$
Total Magnetic Flux	$1.0 \times 10^{21} \text{ Mx}^c$	$4.7 \times 10^{20} \text{ Mx}$
Sheet Thickness / Tube Radius	1000 km	1000 km
Initial Depth	–20,000 km	–20,000 km
Arrival Time at the Surface	$4.9 \times 10^4 \text{ s}$	$2.0 \times 10^4 \text{ s}$
Deceleration Depth	–10,000 km	–5000 km

^aTypical case of Paper I.

^bTypical case of this paper (twist $q = 0.1/H_0$).

^cThe flux sheet is assumed as a prism with a base $1000 \text{ km} \times 10,000 \text{ km}$